

## Article

# Instantaneous Ablation Behavior of Laminated CFRP by High-Power Continuous-Wave Laser Irradiation in Supersonic Wind Tunnel

Te Ma <sup>1,2,†</sup>, Jiangtao Wang <sup>1,†</sup>, Hongwei Song <sup>1,2,3,\*</sup> , Ruixing Wang <sup>1</sup> and Wu Yuan <sup>1</sup>

<sup>1</sup> Key Laboratory for Mechanics in Fluid Solid Coupling Systems, Institute of Mechanics, Chinese Academy of Sciences, Beijing 100190, China

<sup>2</sup> School of Engineering Science, University of Chinese Academy of Sciences, Beijing 100049, China

<sup>3</sup> State Key Laboratory of High-Temperature Gas Dynamics, Institute of Mechanics, Chinese Academy of Sciences, Beijing 100190, China

\* Correspondence: songhw@imech.ac.cn

† These authors contributed equally to this work.

**Abstract:** Experimental and numerical investigations of the instantaneous ablation behavior of laminated carbon fiber-reinforced polymer (CFRP) exposed to an intense continuous-wave (CW) laser in a supersonic wind tunnel are reported. We establish an in situ observation measurement in the experiments to examine the instantaneous ablation behavior. The surface recession depth is calculated by using the Particle Image Velocimetry (PIV) method, taking the ply angle of laminated CFRP as a reference. A coupled thermal-fluid-ablation numerical model incorporating mechanisms of oxidation, sublimation, and thermomechanical erosion is developed to solve the ablation-through problem of multilayer materials. The results show that the laser ablation depth is related to the laser power density, airflow velocity and airflow mode. Thermomechanical erosion is the primary ablation mechanism when the surface temperature is relatively low and the cavity flow mode is a closed cavity flow. When the surface temperature reaches the sublimation of carbon and the airflow mode is transformed to open cavity flow, sublimation plays a dominant role and the ablation rate of thermomechanical erosion gradually decreases.

**Keywords:** laminated CFRP; laser irradiation; in situ observation; instantaneous ablation behavior; coupled thermal-fluid-ablation model



**Citation:** Ma, T.; Wang, J.; Song, H.; Wang, R.; Yuan, W. Instantaneous Ablation Behavior of Laminated CFRP by High-Power Continuous-Wave Laser Irradiation in Supersonic Wind Tunnel. *Materials* **2023**, *16*, 790. <https://doi.org/10.3390/ma16020790>

Academic Editor: Karim Benzarti

Received: 21 December 2022

Revised: 8 January 2023

Accepted: 11 January 2023

Published: 13 January 2023



**Copyright:** © 2023 by the authors. Licensee MDPI, Basel, Switzerland. This article is an open access article distributed under the terms and conditions of the Creative Commons Attribution (CC BY) license (<https://creativecommons.org/licenses/by/4.0/>).

## 1. Introduction

The laminated carbon fiber-reinforced polymer (CFRP) composites have been widely used in industrial sectors, aeronautics and aerospace engineering. The high specific strength, specific stiffness, and excellent designability characteristics of laminated CFRP can significantly improve the performance of high-speed flights such as missiles and unmanned aerial vehicles. However, the thermal damage caused by laser irradiation is a significant threat when the high-power laser becomes an important intercept strategy [1–3].

Under the combined action of laser irradiation and tangential airflow, complex ablation behaviors may occur, such as pyrolysis of the polymer matrix, oxidation and sublimation of residual char and fibers, and thermomechanical erosion. Several works have been reported on the laser ablation of polymer-based composites [4–18]. There are few studies considering the influence of tangential airflow. Recently, we presented the comparative experimental results of the ablation behavior of laminated CFRP in different environments, that is, static nitrogen, stagnant air, open airflow, and tangential supersonic airflow. The thermomechanical erosion (TME) caused by tangential airflow not only increases the total ablation depth at the coupled ablation zone (CAZ) but also converts the heat-affect zone (HAZ) into the downstream affected zone (DAZ) [19]. In our previous work, the

traditional method is used to compare the experimental results of specimens, such as the linear ablation rate, before and after experiments [20–25]. However, the laser ablation process is complex, resulting from the mutual coupling of various ablation mechanisms. The polymer matrix of the CFRP composites undergoes a pyrolysis reaction first and generates the pyrolysis gas and residual char. Fibers that have lost matrix reinforcement are subject to mechanical erosion by tangential airflow. Then, fibers also undergo an oxidation reaction or even a sublimation reaction as the temperature rises. The biggest drawback of the traditional method is failed to provide real-time information about the laser ablation process. Thus, instantaneous data are demanded to analyze the evolution of ablation mechanisms. Some researchers develop real-time ablation methods such as ablation potentiometers, thermocouple arrays, and ultrasonic waves to acquire real-time ablation data. McWhorter et al. [26–28] developed an ablative potentiometer for real-time measurement of ablative characteristics. The thermocouple is embedded in the insulation layer to measure the dynamic ablative process of the head insulation layer. Cauty et al. [29] employed an ultrasonic method to assess the dynamic ablative process of the insulation layer in the engine. Sakai et al. [30] described an ablation sensor that can measure ablation fronts in real-time and in situ, but the measurement is limited to a small region. Martin et al. [31] devised a technique for obtaining real-time X-ray radiography of ablated materials. Qu et al. [32] obtained real-time ablation images using an optoelectronic system for in situ observation and measurement in the arc-heated tunnel test. Tang et al. [33] analyzed the thermal ablation mechanisms of C/SiC composites based on an in situ and real-time optical visualization technique. Zhu et al. [34] used an optical imaging technique to in situ and real-time record the surface evolution of a flat plate subjected to thermal ablation at 1700 °C in a wind tunnel. Nonetheless, the temperature of the specimen under laser irradiation is more extreme. For the indirect measurement method, the high temperature and the laser reflection cause the image to be overexposed, covering up the adequate information of the image. The above experimental methods are insufficient to obtain instantaneous ablative morphology under complex high-temperature environments. Therefore, it is necessary to establish an in situ observation technology that can be applied to the combined action of high-energy laser and wind tunnel to clarify the influences of tangential airflow on laser ablation behaviors.

Meanwhile, the numerical simulation has been a powerful tool to assist the interpretation of the experimental results and reveal the ablation mechanism [35,36]. However, laser irradiation is a particular local ablation and fluid–solid interface recession problem. The traditional method uses Arbitrary LagrangianEulerian (ALE) adaptive remesh algorithm to adjust the location of nodes [37]. Nevertheless, it is unsuitable for laminated CFRP composite (the different material orientations can be performed as one material) due to the ALE method being applicable to single-layer material [38,39]. Furthermore, the coupled thermal-fluid-ablation behaviors become more complex under the combined action of laser irradiation and tangential airflow. For instance, we discovered a unique “avalanche” phenomenon in which the ablation rate under tangential airflow was significantly higher than that in the static air environment for C/SiC composites [40]. The results show that laser ablation has complex coupling behaviors in tangential airflow. The evolution of the laser ablation pit changed the local airflow mode, and the unsteady change of the local aerodynamic force significantly altered the laser ablation behavior. Therefore, a comprehensive coupled thermal-fluid-ablation model that deals with the multilayered ablation-through problem should be established to identify the laser ablation mechanism and analyze the coupling behaviors.

This paper aims to obtain experimentally and numerically the instantaneous ablation behaviors of laminated CFRP. The contribution of various ablation mechanisms to total ablation is revealed. Firstly, an experimental method is developed to measure the instantaneous ablative morphology evolution of the laser irradiation surface of laminated CFRP composites in a supersonic wind tunnel. The experimental method includes an in situ optoelectronic measuring system appropriate for extreme thermal–mechanical conditions.

In addition, Particle Image Velocimetry (PIV) is used as a post-processing method to calculate the surface recession depth (SRD). Then, a coupled thermal-fluid-ablation model is developed to demonstrate the contribution of each ablative mechanism. The Radial Basis Function (RBF) and Remapping Solution Technology (RST) methods are established to simulate the multilayer ablation-through behaviors. The evolution of ablative mechanisms and morphology of multilayered CFRP, when subjected to continuous-wave (CW) laser irradiation and supersonic airflow, are revealed.

## 2. Experimental Setup

### 2.1. Experimental Procedure

The experimental setup is illustrated in Figure 1. An in situ observation measurement consists of a high-speed camera, neutral filter, and narrow-band pass filter. Laser illumination provides background light while avoiding high-energy laser bands with a narrow-band pass filter. The laser device, laser illumination, and high-speed camera are triggered and started simultaneously by a synchroscope during the experiments to ensure sampling consistency.

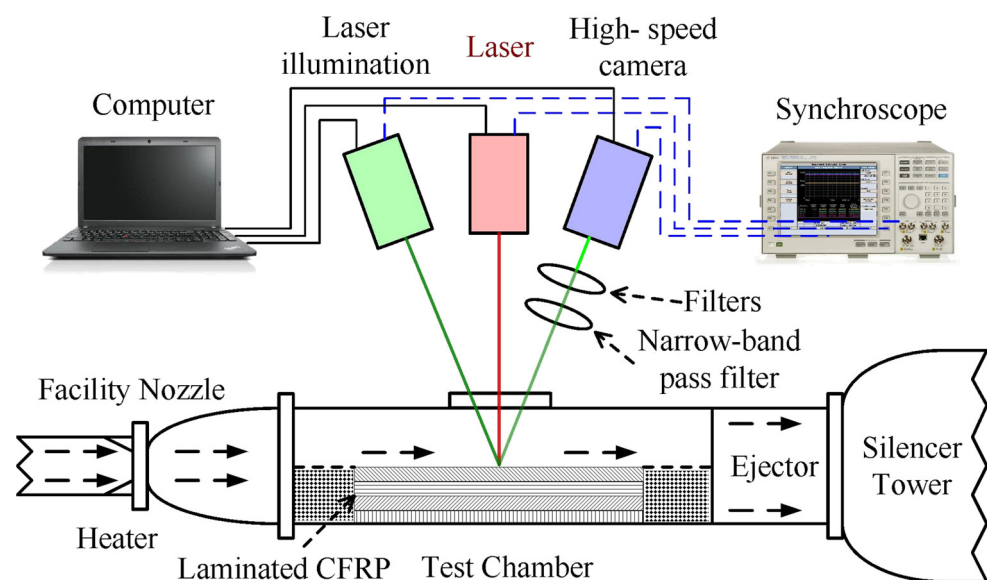


**Figure 1.** Schematic diagram of experimental setup.

The laminated CFRP specimen is placed in the test chamber of a supersonic wind tunnel using a specially designed fixture that ensures the tangential flow of the supersonic free stream over one side of the specimen. During the test, this side is exposed to laser irradiation from a Yb:YLS continuous-wave laser with a wavelength of 1064 nm. The laser beam irradiates the CFRP sample through a high-temperature quartz window. The experiment employs the supersonic wind tunnel facility at the State Key Laboratory of High-Temperature Gas Dynamics (LHD) of the Institute of Mechanics, Chinese Academy of Sciences. It operates on the oxygen-hydrogen combustion principle and can provide a free stream of Mach 1.8 to 4.0 in the test section. The principle of the wind tunnel can also be seen in [19]. In the experiments, tangential supersonic airflow is set as Mach 1.8 and Mach 3.0, respectively. The diameter of the laser spot irradiated on the sample is 10 mm. The laser irradiation time is set as 4.0 s. Two groups of laser parameters, that is, power densities of  $1273 \text{ W/cm}^2$  and  $2546 \text{ W/cm}^2$ , are tested.

Laminated T700/BA9916 CFRP plates with the ply pattern of  $[45^\circ/0^\circ/-45^\circ/90^\circ]_{2S}$  are fabricated and provided by AVIC Composite Corporation Ltd. (Beijing, China). Moreover, BA9916 is a  $180^\circ \text{C}$  high-temperature curing and high-toughness epoxy resin matrix. The detailed preparation process of the specimen can be found in [19]. Table 1 shows the main

physical and mechanical properties of the T700/BA9916 CFRP plates. The samples used in the experiment have dimensions of  $50 \times 50 \times 2.40$  mm and a lamina thickness of 0.15 mm.

**Table 1.** The main physical and mechanical properties of the T700/BA9916 CFRP plates.

Physical Properties (Room Temperature)	Parameter	Mechanical Properties (Room Temperature)	Parameter
Matrix Content (wt%)	$38 \pm 3$	0° Tensile Strength (MPa)	1489
The density of matrix ( $\text{g}/\text{cm}^3$ )	$1.3 \pm 0.04$	0° Tensile Modulus (GPa)	132.8
The density of fiber ( $\text{g}/\text{cm}^3$ )	$1.78 \pm 0.04$	90° Tensile Strength (MPa)	58.5
Volatile Content (%)	$\leq 1.5$	90° Tensile Modulus (GPa)	9.7
Porosity (%)	$\leq 1.5$	Shear Strength (MPa)	121
Lamina Thickness (mm)	$0.15 \pm 0.015$	Shear Modulus (GPa)	5.3

## 2.2. Method of Image Analysis

We use Particle Image Velocimetry (PIV) methods to calculate the fibers' velocity distribution on the laser irradiation surface of the laminated CFRP. In the present paper, the fibers serve as the tracer particles for measuring velocity. As illustrated in Section 2.1, the experimental procedure does not include a particle pattern typically used to visualize fluid motion (either gaseous or liquid). The free, open-source code PIVlab is employed [41], together with a Matlab code that is based on a state-of-the-art multi-pass window deformation algorithm. PIVlab is reported to provide relatively accurate measurements with a random error, typically less than 0.02 pixels/frame, under ideal synthetic images with no noise and no shear. Figure 2 depicts the flowchart of PIVlab 2.02 software.

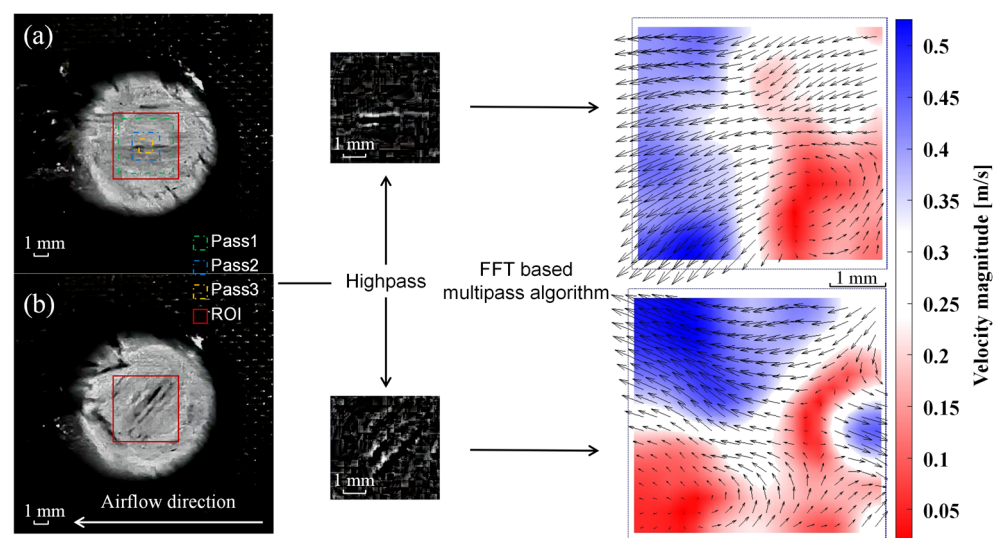


**Figure 2.** The flowchart of PIVlab analysis and results of velocity distribution. (a) Laser irradiation time is 0.8 s; (b) Laser irradiation time is 1.2 s.

After determining and analyzing the size of the ablation pit, the captured images are converted to grayscale images and imported into PIVlab in Matlab R2016a software. An interrogation area of about  $5 \times 5$  mm of the two-dimensional plate is chosen as the region of interest (ROI) to perform the analysis. According to a general recommendation, three passes are used for data analysis, 128 pixels in Pass 1, 64 pixels in Pass 2 and 32 pixels in Pass 3. Inhomogeneous lighting caused by laser irradiation can result in low-frequency background information. It can be eliminated by a high-pass filter that mostly conserves the high-frequency information from particle illumination. The Fast Fourier Transform (FFT) is used to solve the problem in the frequency domain.



### 3. Coupled Thermal-Fluid-Ablation Model

In our previous work, we preliminarily analyzed the thermal-fluid–solid coupling behaviors [19]. The numerical simulation includes a thermomechanical model, linear ablation models, and the heat balance analysis on the ablation surface to determine the ablation depth and clarify the ablation mechanism. Meanwhile, Thermal Gravimetry (TG) and Differential Scanning Calorimetry (DSC) tests are performed to obtain the pyrolysis process of epoxy resin, the oxidation process of carbon fiber, and the reaction heat.

Nevertheless, the previous work equates the laminated CFRP to a macroscopic model and cannot reveal the ablation process through each layer. Each layer has a different ply angle for the multilayer laminated CFRP composite. Therefore, each layer can be treated as a different material, and a more precise model is demanded to examine the ablation behavior. Furthermore, there needs to be more analysis of the relationship between thermomechanical erosion and tangential airflow. In order to solve the above two deficiencies, we further improve the numerical model of the previous work focused on the coupled ablation zone (CAZ).

First, the coupled numerical analysis and the theoretical model are introduced. Figure 3 depicts the flowchart of the coupled thermal-fluid-ablation analysis. The entire analysis consists of three steps. Step 1 is material properties at high temperatures, where a pyrolysis model of the epoxy resin matrix and mass balance are used. Step 2 is thermochemical ablation and thermomechanical erosion analysis, where a linear ablation model and heat balance are used. Step 3 is multi-physics coupling analysis, where the interactive and coupled behavior of ablation, fluid and structure are investigated.

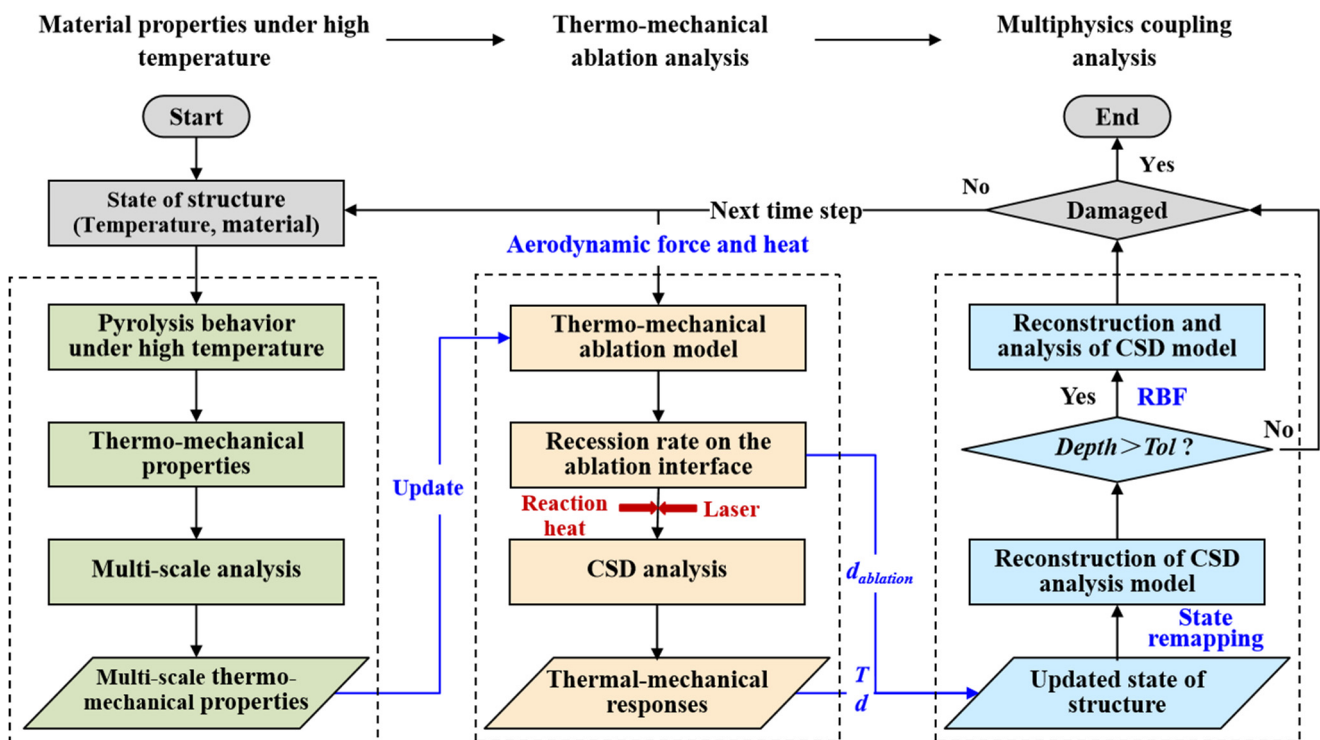


Figure 3. The flowchart of coupled thermal-fluid-ablation analysis.

The fluid and structural solver solve the partition problem independently, and coupling analysis is realized by controlling the data transfer on the fluid–solid boundary. The coupling strategy employs a loosely coupled partitioned strategy to reduce computational efforts by exchanging information less frequently between solvers. Step 1 provides multi-scale thermomechanical properties for Step 2 in each time step to ensure the correctness of HAZ. A multi-scale analysis model to identify the high-temperature parameters can be

identified in [42]. The material content change model can be expressed using Arrhenius functions [19].

$$\frac{\partial \varphi_b}{\partial t} = -J_b \varphi_b^n \exp\left(-\frac{E_{Ab}}{RT_w}\right) \tag{1}$$

$$\frac{\partial \varphi_f}{\partial t} = -J_f [\varphi_f - \varphi_f^0 (1 - \Gamma_f)]^n \exp\left(-\frac{E_{Af}}{RT_w}\right) \tag{2}$$

where  $\varphi$  is the concentration, subscripts  $f$  and  $b$  represent fiber and matrix, respectively,  $E_A$  denotes the apparent energy of activation,  $J$  is the pre-exponential factor,  $t$  is the time,  $\Gamma_f$  is the gasification coefficient of fiber,  $R$  is the universal gas constant, and  $T_w$  is the temperature,  $n$  is the reaction order.

In Step 2, the fluid field transfers the aerodynamic heat flow and pressure to the structure field via the fluid–solid interface (FSI). The following equations calculate the boundary movement of each node caused by linear ablation [19]:

$$v_t = v_o + v_s + v_m \tag{3}$$

$$v_o = \frac{1}{\rho_w} \sum \frac{M_i}{M_{O_2}} p_{O_2}^n A_i \exp\left(-\frac{E_{Ai}}{RT_w}\right) \tag{4}$$

$$v_s = \frac{1}{\rho_w} \left(\frac{\alpha}{c_p}\right) \left(\frac{p_g^*}{p_e}\right) \exp\left(-\frac{E_{AS}}{RT_w}\right) \tag{5}$$

$$v_{m\perp} = \frac{1}{\rho_f} \left(\frac{J_f^0 k_f}{c_f}\right)^{1/2} \left(\frac{6p_\Sigma}{\sigma_{f\perp}}\right)^{3/2} \left(\frac{RT_w}{E_{Af}}\right)^{1/2} \exp\left(-\frac{E_{Aft}}{RT_w}\right), v_{m\parallel} = v_{m\perp} \left(\frac{\sigma_{f\perp}}{\sigma_f}\right)^{1/2} \tag{6}$$

where  $v_t$  is the total linear rate,  $v_o$  is the oxidation rate,  $v_s$  is the sublimation rate,  $v_m$  is the mechanical erosion rate,  $\rho_w$  is the density of the laminated CFRP,  $M_i$  is the average molecular mass of the substance  $i$  involved in the oxidation reaction,  $M_{O_2}$  is the molecular mass of oxygen,  $p_{O_2}$  is the partial pressure of oxygen in the airflow,  $A_i$  is the pre-exponential factor of oxidation reaction,  $\alpha/c_p$  is the heat transfer coefficient,  $p_g^*$  is the gas pressure constant,  $p_e$  is the local pressure,  $p_\Sigma$  is the pressure head of airflow on the ablation surface,  $\sigma_f$  and  $\sigma_{f\perp}$  denotes the strength of mono-fiber in the longitudinal and perpendicular directions, respectively.

It is necessary to consider processes of heat and mass transfer occurring on the surface. The net conduction heat flux can be obtained from thermal equilibrium in the ablation boundary:

$$-\lambda \frac{\partial T_w}{\partial n} = \alpha q_{\text{laser}} - q_{\text{rad}} - q_{\text{conv}} + q_{\text{oxi}} - q_{\text{deg}} - q_{\text{phas}} \tag{7}$$

where  $\alpha$  is the absorption coefficient,  $q_{\text{laser}}$  is the heat flux of the laser,  $q_{\text{rad}}$ ,  $q_{\text{conv}}$ ,  $q_{\text{oxi}}$ ,  $q_{\text{deg}}$  and  $q_{\text{phas}}$  are the heat flux due to surface radiation, convection between composites and airflow, oxidation of residual carbon and fiber, decomposition and pyrolysis of epoxy resin, and phase change and sublimation, respectively. Additionally,  $q_{\text{rad}} = \varepsilon \sigma (T_w^4 - T_0^4)$  where  $\varepsilon$  is the emissivity of the ablation surface,  $\sigma$  is a Stefan–Boltzmann constant and  $T_0$  is the environment airflow temperature.  $q_{\text{conv}} = h_w (T_w - T_0)$  where  $h_w$  is the coefficient of convective heat transfer.  $q_{\text{deg}} = Q_0 \frac{\partial m}{\partial t} - V (\varphi_g \rho_g \vec{v}_g) \cdot \nabla h_g$  where  $Q_0$  is the endothermic heat of degradation from the unit mass of the composite. The second part is the convective heat taken away by pyrolysis gas.  $V$  is the volume of the composite,  $h_g$  is the enthalpy of the pyrolysis gas,  $\rho_g$  is the density of the pyrolysis gas,  $\vec{v}_g$  is the velocity vector of the gas flow,  $c_g$  is the specific heat of the pyrolysis gas.  $q_{\text{oxi}} = C_{bef} \Delta H_{bef} - C_{aft} \Delta H_{aft}$  where  $C_i$  is the mass concentration of the component,  $\Delta H_i$  is the enthalpy of components.  $q_{\text{phas}} = \sum m_i \int_{T_s}^{T_s} c_i dT$  where  $m_i$  is the mass of components occurring phase changes, and  $c_i$

is the specific heat of corresponding components. In this paper, the phase change processes of the pyrolytic residual char and carbon fibers are mainly considered.

The deformed meshes are adjusted by Radial Basis Function (RBF) in Step 3, then the Remapping Solution Technology (RST) variables from the old mesh to the new mesh with a process called advection. The principle is that the actual spatial distribution of the material properties and state variables in the old mesh is mapped to the new mesh that has been adjusted for recession. It can deal with the mesh is not allowed to flow from one material domain to another when the material is multilayer. The flowchart of the adaptive mesh algorithm for multilayer material can be shown in Figure 4. The iterative partitioned solution method must solve each single field problem several times until the equilibrium condition is satisfied before moving on to the next time step calculation. The conservation and continuity of all physical quantities transferred at the fluid–solid interface (FSI), including temperature, heat flow, and deformation, are strictly guaranteed.

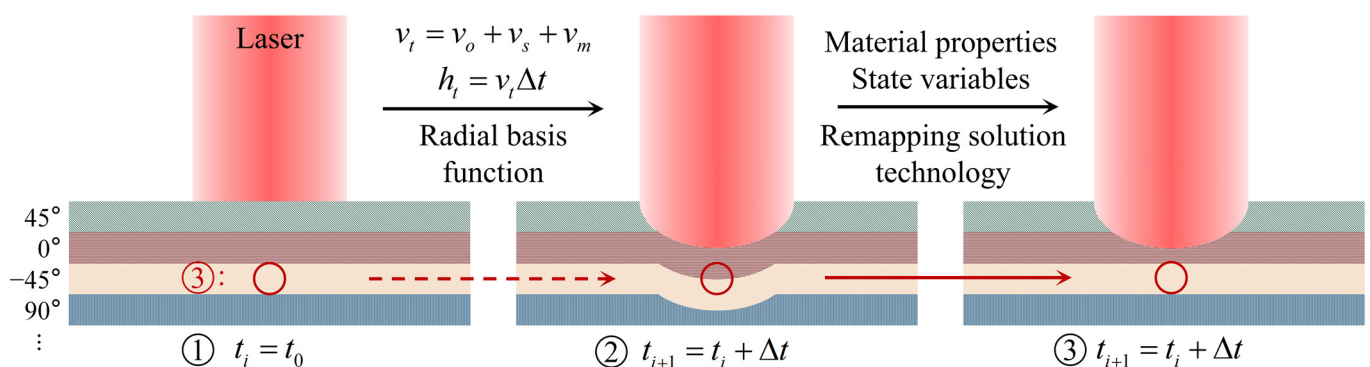


**Figure 4.** The flowchart of adaptive mesh algorithm for multilayer material.

Then, the numerical modeling is introduced in the following. The three-dimensional parameter of the solid numerical model is  $50 \times 50 \times 2.40$  mm. It is modeled according to the ply pattern of the experimental specimen  $[45^\circ/0^\circ/-45^\circ/90^\circ]_{2S}$ , which contains 16 layers in total, and the thickness of each layer is 0.15 mm. C3D8 8-node linear hexahedron element is used. The number of nodes is 313,638, and the number of elements is 259,200. The fluid numerical model has dimensions of  $150 \times 120 \times 50$  mm. It has meshed with a structural grid of  $150 \times 81 \times 152$  nodes. The grid near the wall is refined to 0.01 mm in the normal direction and 0.2 mm in the streamlined direction. The boundary conditions are established and named inlet, far field, outlet, no-slip wall, and symmetry.

## 4. Results and Discussions

### 4.1. Experimental Results and Parameters' Influence

Figure 5 exhibits the instantaneous ablation morphology of the laser irradiation surface when the laser power density is  $1273 \text{ W/cm}^2$  and the Mach number is 3.0. The real-time distributions of carbon fiber can be clearly seen in Figure 5, such as the ply angel being  $45^\circ$ ,  $0^\circ$ ,  $-45^\circ$ , and  $90^\circ$ , respectively. The experimental results demonstrate vast potential for using this in situ measuring technique in extreme thermal–mechanical conditions. On the one hand, the ablation process of material can be clarified. On the other hand, real-time ablation information can be obtained based on the post-process of the experimental data.

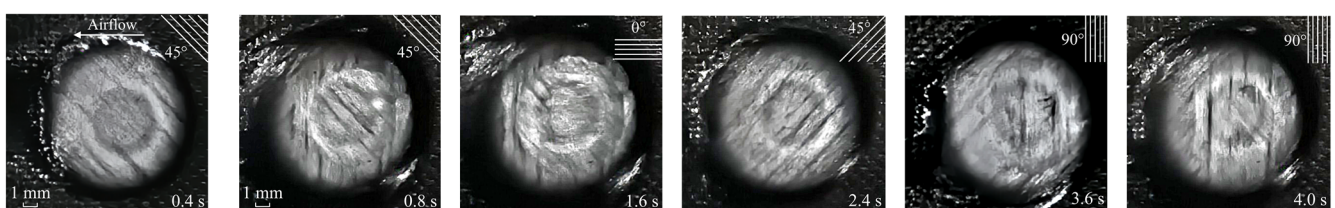


**Figure 5.** The instantaneous ablation morphology of laser irradiation surface.



Figure 6 shows the comparisons of laser ablation morphology at different conditions. Meanwhile, Figure 7 gives the instantaneous surface recession depth curve that is calculated by using PIVlab results when the velocity direction is transformed, which helps explain the process of real-time ablation in more detail.

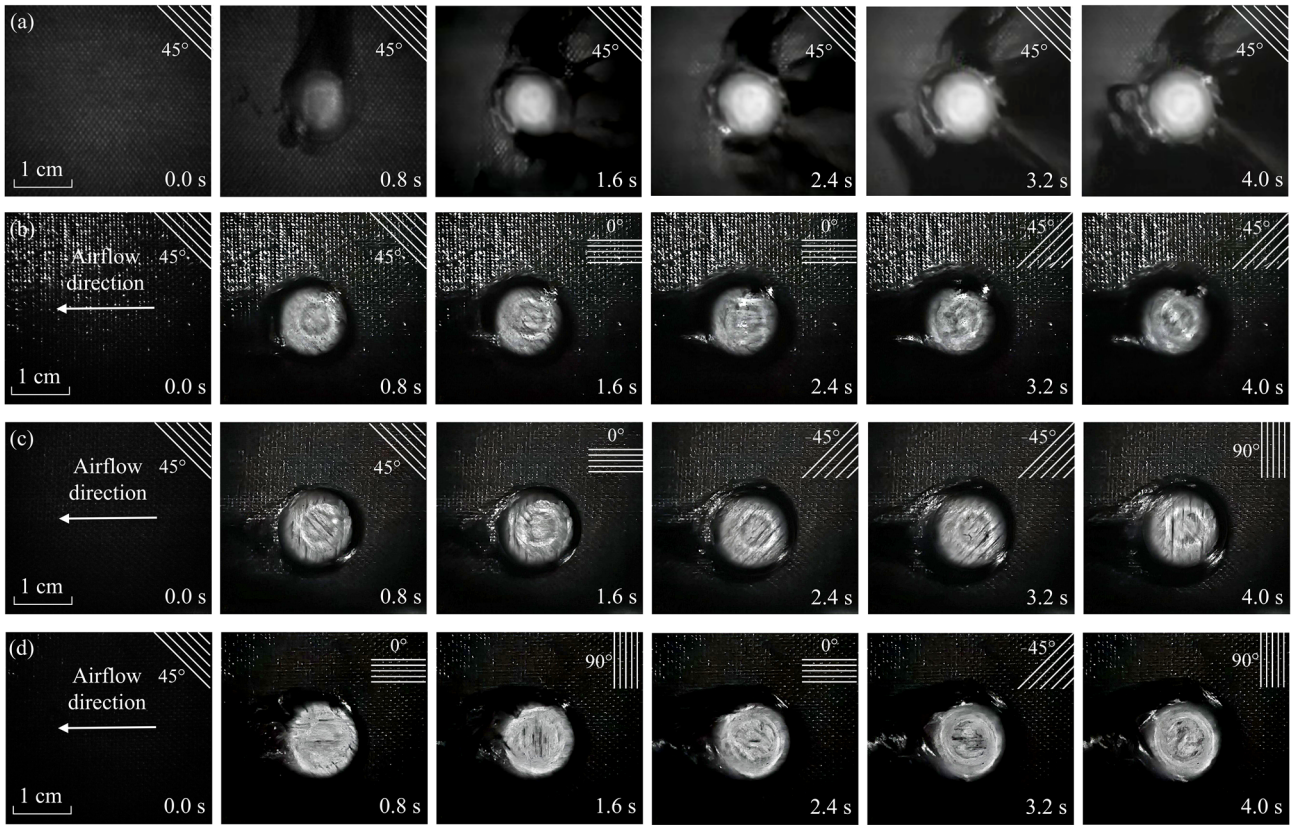


Figure 6. The laser irradiation process in different conditions. (a) Static air, 1273 W/cm<sup>2</sup>; (b) Ma 1.8, 1273 W/cm<sup>2</sup>; (c) Ma 3.0, 1273 W/cm<sup>2</sup>; (d) Ma 3.0, 2546 W/cm<sup>2</sup>.

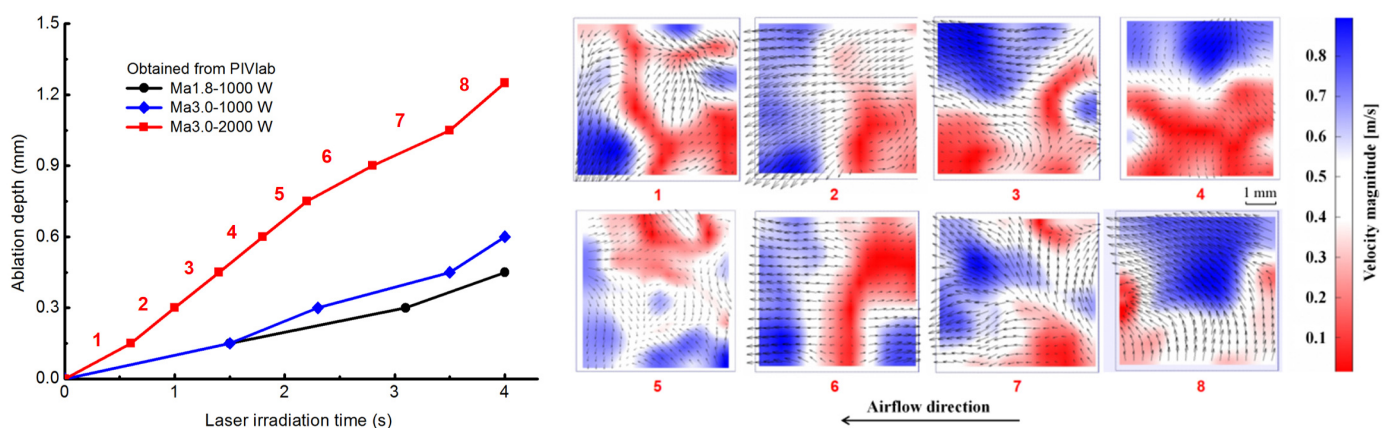


Figure 7. Instantaneous surface recession depths of different experimental conditions are obtained by PIVlab analysis.

Figure 6a depicts the real-time laser ablation morphology of laminated CFRP in a static air environment with a power density of 1273 W/cm<sup>2</sup>. The pyrolysis of epoxy resin matrix on the laser irradiation surface occurs immediately after laser irradiation, resulting in the formation of soot, including the residual carbon. Typically, it includes those progress from cured resin to dehydrated resin to decomposition and char oxidation to leave bare carbon

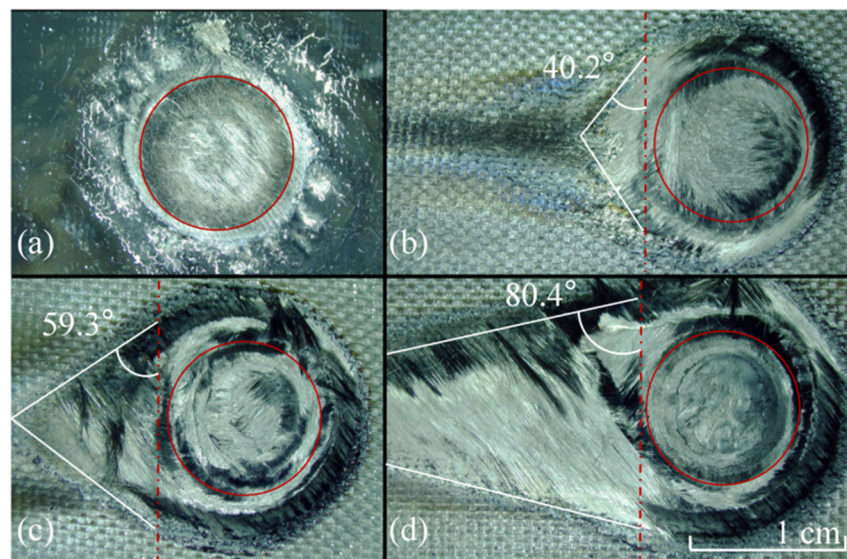
fiber [43–45]. However, the soot is rapidly produced when the laser irradiation time is only 0.1 ms. This phenomenon illustrates that the transformation of the first progress is quick, so the dehydrated stage is ignored in this work. The heat-affected zone (HAZ) is elliptical due to its anisotropic thermophysical properties. The central area becomes bright, and the HAZ reverts to a circular shape because of the ever-increasing temperature. The direction of the fibers does not change throughout the laser ablation process, indicating that this layer is yet ablated-through, and the fibers do not undergo oxidation or sublimation reaction.

Figure 6b shows the real-time ablation process of CFRP composites at Mach 1.8 with a power density of  $1273 \text{ W/cm}^2$ . The tangential supersonic airflow changes the ablation behaviors of the laser irradiation region. HAZ is not an apparent ellipse. Convective cooling of tangential supersonic airflow is primarily responsible for this phenomenon. Furthermore, as shown in Figure 7, the ply angle of fibers on the laser irradiation surface shifts from  $45^\circ$  to  $0^\circ$  after 1.5 s of laser irradiation. The transition from  $0^\circ$  to  $-45^\circ$  ply angle lasts 3.1 s.

Figure 6c illustrates the ablation process under the tangential airflow velocity of Mach 3.0 with a power density of  $1273 \text{ W/cm}^2$ . According to Figures 6c and 7, the laminate with a ply angle of  $45^\circ$  (see the fiber direction) lasts up to 1.4 s. The above results demonstrate that the increase in the airflow velocity does not significantly improve mechanical erosion efficiency, much attributed to the low-temperature field in the early stage of laser irradiation. Then the laminate with a ply angle of  $0^\circ$  lasts for 0.9 s (2.3 s in total), the  $-45^\circ$  laminate lasts for 1.2 s (3.5 s in total), and the fibers transform to  $90^\circ$ . It should be noted that the final laser ablation depth (LAD) should be corrected by post-test measurement since the last frame of the velocity field has no reference. The above findings show that the TME effect intensifies with the increased temperature, proving that mechanical erosion is a thermal–mechanical coupling behavior. As the laser power density rises to  $2546 \text{ W/cm}^2$ , the fiber direction rapidly changes, as illustrated in Figures 6d and 7. The ablation-through of the first laminate needs only 0.6 s. At 4.0 s, a total of 8 layers are ablation-through. The ablation depth is at least twice that of  $1273 \text{ W/cm}^2$ .

Detailed post-irradiated samples are given in Figure 8. The laser ablation area can be divided into two regions: the coupled ablation zone (CAZ) and downstream affected zone (DAZ). In CAZ, the uppermost ablative character is the laser ablation pit, which is caused by laser irradiation and high-speed airflow. Although the laser does not irradiate DAZ directly, it still forms tail-shape damage. The matrix begins to pyrolyze when the heat-affected zone expands to DAZ. Meanwhile, fibers without the immobilization of the matrix are formed the damaged morphology under tangential airflow. The tail-shape damage degree is also related to the laser power density and the airflow velocity, and we can use the tail-shape angle to characterize it. As can be seen in Figure 8b, the tail-shape angle is  $40.2^\circ$ . When the tangential airflow increases to Ma 3.0, the angle rises to  $59.3^\circ$ . As the laser power density increases to  $2546 \text{ W/cm}^2$ , the angle rises to  $80.4^\circ$ .





Downstream affected zone (DAZ) ← : : → Coupled ablation zone (CAZ)

**Figure 8.** The laser ablation morphology in different condition. (a) Static air; (b) Ma 1.8, 1273 W/cm<sup>2</sup>; (c) Ma 3.0, 1273 W/cm<sup>2</sup>; (d) Ma 3.0, 2546 W/cm<sup>2</sup>.

#### 4.2. Numerical Results and Ablation Mechanisms

As illustrated in Figure 9, the evolution of laser ablation morphology obtained by numerical simulation is compared with the experimental results when the laser power density is 2546 W/cm<sup>2</sup> and the Mach number is 3.0. The material parameters are given in Appendix A—Table A1. The laser absorption of CFRP is 0.9 when the laser wavelength is 1064 nm [46]. In Figure 9b, each color represents a different ply angle. The coupled thermal-fluid-ablation model using RBF and RST methods can effectively solve multilayer elements' laser ablation morphology evolution. As a result, the numerical calculation of the ablative process corresponds to experimental results.

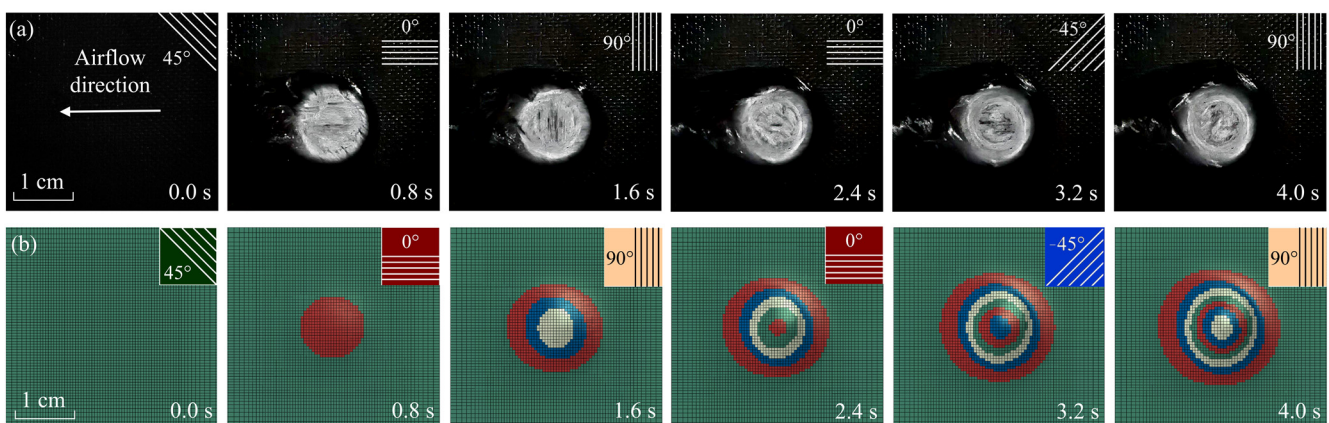


**Figure 9.** The ablative morphology at different times. (a) Experimental results; (b) numerical results.

A Bruker (Karlsruhe, Germany) DektakXT profiling system scans the samples to investigate the ablation pit (Figure 10a). The comparison of experimental and numerical results at the final laser irradiation time is illustrated in Figure 10a. The ablation depths of each numerical case agree with those of experimental results at the laser irradiation center. The numerical results of ablation depth are 0.38 mm, 0.44 mm, and 1.13 mm, and the corresponding experimental results are 0.36 mm, 0.47 mm, and 1.07 mm, with errors of 5.56%, −6.38%, and 5.61%, respectively, for the cases of laser power density 1273 W/cm<sup>2</sup> and Mach 1.8, laser power density 1273 W/cm<sup>2</sup> and Mach 3.0, the laser power density is

2546 W/cm<sup>2</sup> and Mach 3.0. The ablative profiles are wavy in experimental results and become more evident with the increased laser power density. This phenomenon is related to the microstructure and different ablation rates of each component of the CFRP composite. The result exemplifies the complex non-linear local ablation. Meanwhile, scanning profiles are used to modify the final real-time ablation depth obtained with PIVlab. The SRD curves then become complete. Experimental results indicate that laser power density is the most crucial parameter for laser ablation depth in the range of tangential supersonic airflow. Moreover, the numerical results are consistent with the experimental results. In this view, real-time SRD curves can be used to validate the numerical model from the whole ablation process rather than just the final ablation depth.

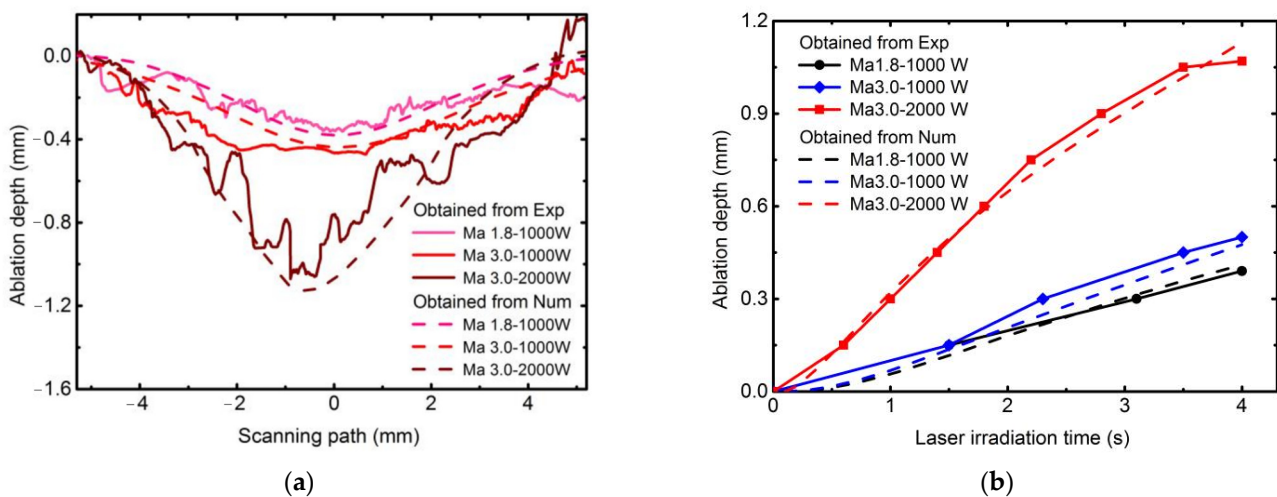


**Figure 10.** Comparison of experimental and numerical results. (a) Profile over the ablation surface; (b) instantaneous ablation depth.

The ablation depth caused by each ablation mechanism at the center of the ablation pit is shown in Figure 11. When the laser irradiation time (LIT) is 4.0 s, the contribution of the sublimation to the total depth is 54.36%, mechanical erosion is 36.54%, and oxidation is 9.1% (Figure 11a). However, when the LIT is less than 2.4 s, mechanical erosion dominates total ablation. The primary reason is that the residual char and fiber begin to strip due to the aerodynamic force of tangential supersonic airflow after the matrix has been pyrolyzed and sublimated. Figure 11b shows the ablation rate curves of each ablative mechanism, providing additional information. The temperature is around 3000 K during the initial stage of laser irradiation (LIT is before 1.5 s). The sublimation rate of carbon fiber and pyrolytic residual carbon is slow in this temperature range, but pyrolysis and matrix sublimation are rapid. The fibers are exposed to tangential supersonic airflow due to losing the bonding function of the matrix. The strength of fibers decreases significantly at high temperatures. As such, the TME rate is faster than the other mechanisms. When the temperature rises to 3300 K, the sublimation rate is accelerated.

It is also observed that there is a transition point in Figure 11b. This is caused by the evolution of ablation morphology, which potentially influences the airflow characteristics. The surface change of the ablation pit is a significant factor influencing the thermomechanical erosion rate. It can be treated as a cavity flow problem [47]. Figure 12 depicts the contours and streamlines of flow velocity and static pressure as ablation morphology evolution. As the ablation depth increases, the cavity flow mode shifts from a closed to an open-cavity regime. There is no significant backward-facing and forward-facing step flow with the impingement of the incoming upstream flow on the cavity wall due to the smooth curved geometry of the ablated pit (Figure 12a,f).

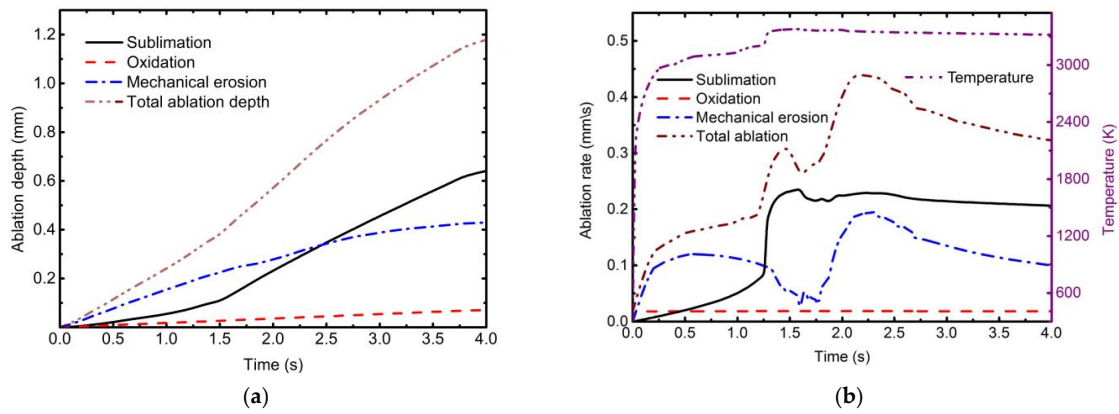


**Figure 11.** The effect of thermochemical ablation and thermomechanical erosion on laser ablation when laser power density is  $2546 \text{ W/cm}^2$  and Mach number is 3.0. (a) Ablation depths; (b) ablation rates.

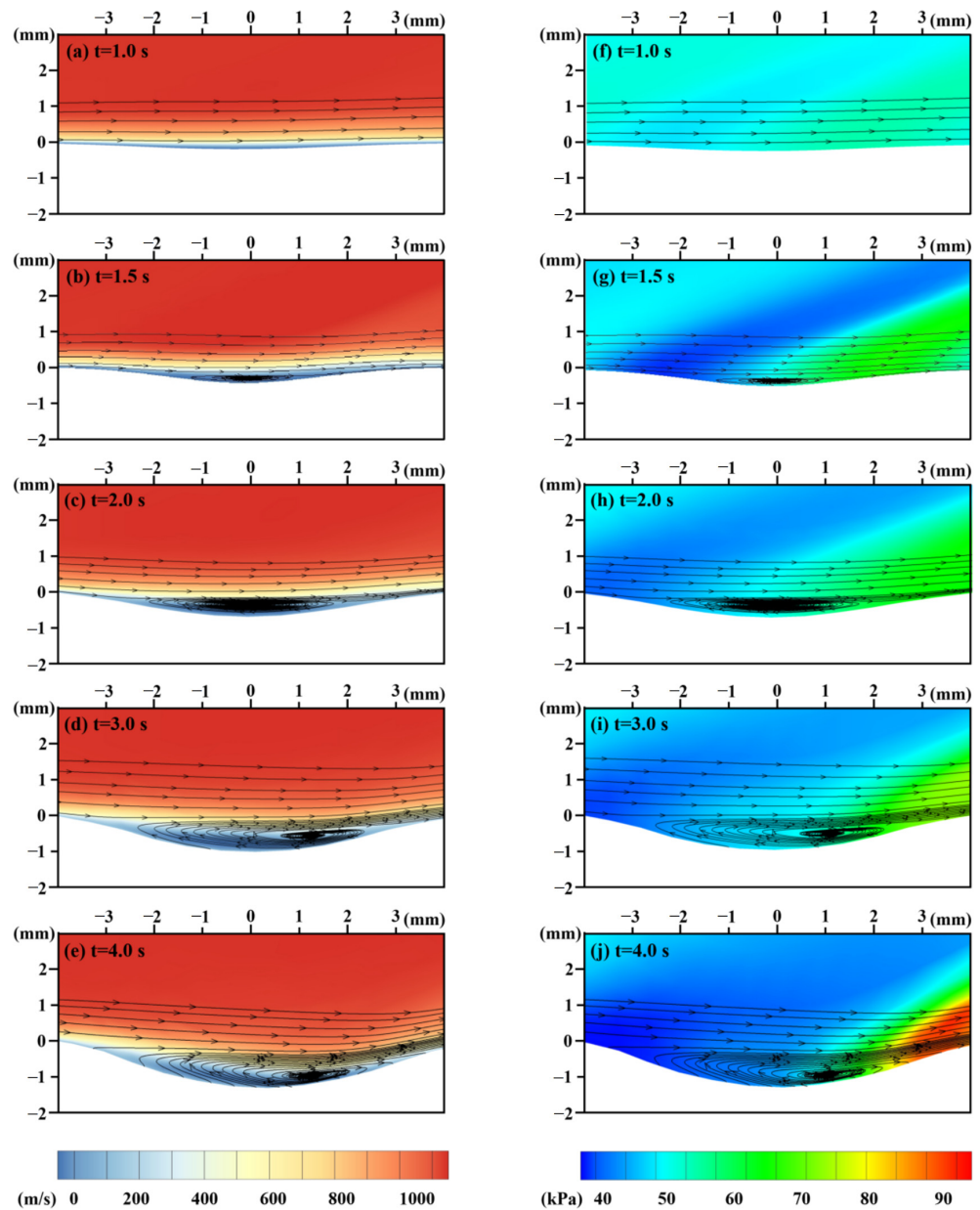


**Figure 12.** The contours and streamlines of flow velocity and pressure in the fluid domain.



When the open cavity flow is formed (Figure 12b,g, with a start time of about 1.5 s), the free stream flow does not directly enter the ablation pit. A shear layer forms between the free stream and the flow inside the pit. This phenomenon results in a transition point. The shear layer extends the length of the pit and makes contact with the aft wall, causing airflow compression and high-intensity static pressure. Because of the high-intensity static pressure, the erosion rates of the backward-facing region become more significant than those of the forward-facing region. Therefore, as illustrated in Figure 12d,e, the vortex inside the ablated pit moves downstream with the laser ablation process.

## 5. Conclusions

The developed experimental measurement and data processing algorithm can effectively characterize real-time laser ablation behaviors and the surface recession depth (SRD) in a high-speed wind tunnel environment. In addition, a coupled thermal-fluid-ablation model, which deals with the ablative deformation of multilayer materials, was developed to obtain the evolution of ablation morphology and examine each ablation mechanism's contribution to the total ablation and the influence of flow regime on the TME. The main findings of the study are summarized as follows:

- (1) In the experimental results, the real-time laser ablation behaviors of CFRP composite illustrate that the TME is a thermal–mechanical behavior. It is related to laser power density and tangential airflow velocity.
- (2) The velocity distribution of carbon fibers was characterized using an open-source PIVlab. The transform of velocity direction obtains the surface recession depth (SRD).
- (3) A coupled thermal-fluid-ablation model was established to demonstrate the effect of the flow regime on the TME. When the laser power density is 2546 W/cm<sup>2</sup> and the Mach number is 3.0, TME dominates total ablation before the laser irradiation time is 2.4 s. When the LIT was 4.0 s, sublimation contributed 54.36% to the total depth, thermomechanical erosion contributed 36.54%, and oxidation contributed 9.10%.
- (4) The numerical results show that TME is related to the temperature and velocity of tangential airflow and the cavity flow mode. When the mode shifts from the closed cavity regime to the open-cavity regime, the transition moment is revealed by the TME curve. Then sublimation plays a dominant role and the ablation rate of TME gradually decreases.

**Author Contributions:** T.M.: Investigation Conducting, Software Programming, Data Curation, Writing—Original Draft. J.W.: Investigation Conducting, Experimental System Construction, Writing—Original Draft. H.S.: Conceptualization, Supervision, Writing—Review & Editing, Project administration. R.W.: Investigation, Software Programming. W.Y.: Investigation, Experimental Assistance. All authors have read and agreed to the published version of the manuscript.

**Funding:** Financial supports from National Natural Science Foundation of China (Grant Nos. 11902322, 11972035, 11972033 and 12102434) are gratefully acknowledged.

**Acknowledgments:** The authors would like to express their appreciation to Hongbin Gu at the State Key Laboratory of high-temperature Gas Dynamics (LHD), Chinese Academy of Sciences, for providing and assisting the supersonic wind tunnel experiments.

**Conflicts of Interest:** The authors declare no conflict of interest.

## Appendix A

**Table A1.** The initial parameters in the coupled thermal-fluid-ablation model.

No.	Symbol	Implication	Unit (mm)	Value
1	$\rho_b$	The density of matrix	ton·mm <sup>-3</sup>	$1.2 \times 10^{-9}$
2	$E_{Ab}$	The activation energy of matrix	mJ·ton <sup>-1</sup>	$1.75 \times 10^5$
3	$J_{0b}$	The pre-exponential factor of matrix	ton·mm <sup>-3</sup> ·s <sup>-1</sup>	$6 \times 10^{-6}$

Table A1. Cont.

No.	Symbol	Implication	Unit (mm)	Value
4	$\phi_b^0$	The concentration of matrix	None	0.97
5	$k_{b0}$	The conductivity of matrix	$\text{mW}\cdot\text{mm}^{-1}\cdot\text{K}^{-1}$	0.35
6	$c_{pb0}$	The specific heat of matrix	$\text{mJ}\cdot\text{ton}^{-1}\cdot\text{K}^{-1}$	$1.2 \times 10^9$
7	$\rho_p$	The density of pyrolytic carbon	$\text{ton}\cdot\text{mm}^{-3}$	$2 \times 10^{-9}$
8	$\phi_p^0$	The concentration of pyrolytic carbon	None	0
9	$k_{p0}$	The conductivity of pyrolytic carbon	$\text{mW}\cdot\text{mm}^{-1}\cdot\text{K}^{-1}$	5
10	$c_{pp0}$	The specific heat of pyrolytic carbon	$\text{mJ}\cdot\text{ton}^{-1}\cdot\text{K}^{-1}$	$6 \times 10^8$
11	$Q_b$	The reaction heat of the pyrolysis	$\text{mJ}\cdot\text{ton}^{-1}$	$7.37 \times 10^{12}$
12	$\rho_f$	The density of carbon fiber	$\text{ton}\cdot\text{mm}^{-3}$	$2.5 \times 10^{-9}$
13	$E_{Af}$	The activation energy of carbon fiber	$\text{mJ}\cdot\text{ton}^{-1}$	$2 \times 10^5$
14	$J_{of}$	The pre-exponential factor of carbon fiber	$\text{ton}\cdot\text{mm}^{-3}\cdot\text{s}^{-1}$	$4.2 \times 10^{-6}$
15	$\Gamma_f$	The gasification coefficient of carbon fiber	None	0.1
16	$\phi_f^0$	The concentration of carbon fiber	None	1
17	$k_{f0}$	The conductivity of carbon fiber	$\text{mW}\cdot\text{mm}^{-1}\cdot\text{K}^{-1}$	42
18	$c_{fb0}$	The specific heat of carbon fiber	$\text{mJ}\cdot\text{ton}^{-1}\cdot\text{K}^{-1}$	$8.9 \times 10^8$
19	$\rho_l$	The density of crystalline phase	$\text{ton}\cdot\text{mm}^{-3}$	$2.5 \times 10^{-11}$
20	$\phi_l^0$	The concentration of crystalline phase	None	0
21	$k_{l0}$	The conductivity of crystalline phase	$\text{mW}\cdot\text{mm}^{-1}\cdot\text{K}^{-1}$	42
22	$c_{pl0}$	The specific heat of crystalline phase	$\text{mJ}\cdot\text{ton}^{-1}\cdot\text{K}^{-1}$	$8.9 \times 10^8$
23	$\phi_{fuc}^0$	The initial volume percent of matrix	None	0.38
24	$\phi_{fuc}$	The initial volume percent of carbon fiber	None	0.62
25	$E_{AS}$	The activation energy of the sublimation reaction	$\text{mJ}\cdot\text{ton}^{-1}$	$2.04 \times 10^5$
27	$A_i$	The pre-exponential multiplier of the oxidation action	$\text{ton}\cdot\text{mm}^{-3}\cdot\text{s}^{-1}$	$5 \times 10^{-10}$
28	$E_{Ai}$	The activation energy of the oxidation reaction	$\text{mJ}\cdot\text{ton}^{-1}$	$2.51 \times 10^4$
31	$J_f^0$	The pre-exponential multiplier of the thermomechanical erosion	$\text{ton}\cdot\text{mm}^{-3}\cdot\text{s}^{-1}$	$5.4 \times 10^{-10}$
33	$\sigma_f, \sigma_{f\perp}$	The strengths of carbon fiber in the longitudinal and perpendicular directions, respectively	MPa	2200, 220
34	$E_{Aft}$	The activation energy of the thermomechanical erosion	$\text{mJ}\cdot\text{ton}^{-1}$	$5.82 \times 10^4$
35	$n$	The reaction order	None	3

## References

- Zhang, Y.X.; Zhu, Z.; Joseph, R.; Shihan, I.J. Damage to aircraft composite structures caused by directed energy system: A literature review. *Def. Technol.* **2021**, *17*, 1269–1288. [\[CrossRef\]](#)
- Candan, C.; Seymen, A.A.; Karatutlu, A.; Tiken, M.; Midilli, Y.; Orhan, E.; Berberoglu, H.; Ortaç, B. Performance evaluation of fiber-based ballistic composites against laser threats. *Optic. Laser. Eng.* **2019**, *121*, 54–60. [\[CrossRef\]](#)
- Garcia, J.D.; Joyce, P.; Brownell, C. Thermal damage behind HEL-irradiated carbon fiber reinforced polymer skin. *J. Directed Energy* **2017**, *6*, 119–136.
- Sun, C.C.; Min, J.Y.; Lin, J.P.; Wan, H.L.; Yang, S.L.; Wang, S. The effect of laser ablation treatment on the chemistry, morphology and bonding strength of CFRP joints. *Int. J. Adhes Adhes* **2018**, *84*, 325–334. [\[CrossRef\]](#)
- Xu, L.Y.; Lu, J.R.; Li, K.M.; Hu, J. Removal mechanism of CFRP by laser multi direction interaction. *Opt. Laser. Technol.* **2021**, *143*, 107281. [\[CrossRef\]](#)
- Pudasaini, S.P.; Fischer, J.T. A mechanical erosion model for two-phase mass flows. *Int. J. Multiph. Flow* **2020**, *132*, 103416. [\[CrossRef\]](#)
- Xu, H.B.; Hu, J. Modeling of the material removal and heat affected zone formation in CFRP short pulsed laser processing. *Appl. Math. Model.* **2017**, *46*, 354–364. [\[CrossRef\]](#)
- Li, J.; Liu, K.; Guo, M.F.; Liu, Y.; Wang, J.; Lv, X. Ablation and erosion characteristics of EPDM composites under SRM operating conditions. *Compos. Part A Appl. Sci. Manuf.* **2018**, *109*, 392–401. [\[CrossRef\]](#)
- Herr, N.C.; Gonzales, A.E.; Perram, G.P. Kinetics, evolving thermal properties, and surface ignition of carbon fiber reinforced epoxy composite during laser induced decomposition. *Polym. Degrad. Stabil.* **2018**, *152*, 147–161. [\[CrossRef\]](#)
- Xu, L.Y.; Lu, J.R.; Li, K.M.; Hu, J. Study on the mechanism of inhomogeneous microdamage in short-pulse laser processing of carbon fiber reinforced plastic. *J. Reinf. Plast. Comp.* **2021**, *40*, 568–576. [\[CrossRef\]](#)
- Wang, S.; Echeverr, Y.J.; Trevisi, L. Ultrahigh Resolution Pulsed Laser-Induced Photoacoustic Detection of Multi-Scale Damage in CFRP Composites. *Appl. Sci.* **2020**, *10*, 2106. [\[CrossRef\]](#)



12. Gebauer, J.; Burkhardt, M.; Franke, V.; Lasagni, A.F. On the Ablation Behavior of Carbon Fiber-Reinforced Plastics during Laser Surface Treatment Using Pulsed Lasers. *Materials* **2020**, *13*, 5682. [[CrossRef](#)] [[PubMed](#)]
13. Niino, H.; Harada, Y.; Fujisaki, A. Thermal Damage of Carbon Fiber Reinforced Plastic by IR Fiber Laser Irradiation. *J. Laser. Micro. Nanoen.* **2017**, *12*, 235–238.
14. Allheily, V.; Lacroix, F.; Eichhorn, A.; Merlat, L.; L'Hostis, G.; Durand, B. An experimental method to assess the thermo-mechanical damage of CFRP subjected to a highly energetic 1.07  $\mu\text{m}$ -wavelength laser irradiation. *Compos. Part B-Eng.* **2016**, *92*, 326–331. [[CrossRef](#)]
15. Li, M.J.; Chen, L.M.; Yang, X.J. A feasibility study on high-power fiber laser cutting of thick CFRP laminates using single-pass strategy. *Opt. Laser. Technol.* **2021**, *138*, 106889. [[CrossRef](#)]
16. Li, X.; Hou, W.T.; Han, B.; Xu, L.F.; Li, Z.W.; Nan, P.Y.; Ni, X.W. Thermal response during volumetric ablation of carbon fiber composites under a high intensity continuous laser irradiation. *Surf. Interfaces* **2021**, *23*, 101032. [[CrossRef](#)]
17. Zhang, J.; Bi, R.; Jiang, S.; Wen, Z.; Luo, C.; Yao, J.; Liu, G.; Chen, C.; Wang, M. Laser Ablation Mechanism and Performance of Carbon Fiber-Reinforced Poly Aryl Ether Ketone (PAEK) Composites. *Polymers* **2022**, *14*, 2676. [[CrossRef](#)]
18. Ohkubo, T.; Sato, Y.; Matsunaga, E.; Tsukamoto, M. Thermal effect of laser ablation on the surface of carbon fiber reinforced plastic during laser processing. *Appl. Phys. A* **2018**, *124*, 149. [[CrossRef](#)]
19. Zhao, W.N.; Ma, T.; Song, H.W.; Yu, W.; Wang, R.X.; Wang, Z. Effects of tangential supersonic airflow on the laser ablation of laminated CFRP. *J. Mater. Res. Technol.* **2021**, *14*, 1985–1997. [[CrossRef](#)]
20. Wang, H.H.; Kong, J.A.; Xu, M.; Zhang, P.F.; Yang, L.; Shi, X.H.; Li, H.J. Laser ablation behavior of  $\text{SiO}_2\text{-Nd}_2\text{O}_3/\text{Si-SiC-MoSi}_2$  coated C/C composites repaired by laser cladding. *Corros. Sci.* **2022**, *198*, 110132. [[CrossRef](#)]
21. Shen, P.F.; Zhuang, Y.P.; Jiang, S.D.; Luo, C.Y.; Tong, X.P.; Liang, Y.Y.; Yan, Y.; Zhang, N.H.; Zhang, L.Y. Experimental and numerical investigation on the ablation mechanism of  $\text{Al}_2\text{O}_3/\text{Al}_2\text{O}_3\text{-CMCs}$  under continuous-wave laser irradiation. *J. Eur. Ceram. Soc.* **2022**, *42*, 2307–2318. [[CrossRef](#)]
22. Fang, X.; Liu, F.; Su, H.; Liu, B.; Feng, X. Ablation of C/SiC, C/SiC– $\text{ZrO}_2$  and C/SiC– $\text{ZrB}_2$  Composites in Dry Air and Air Mixed with Water Vapor. *Ceram. Int.* **2014**, *40*, 2985–2991. [[CrossRef](#)]
23. Badhe, Y.; Balasubramanian, K. Novel Hybrid Ablative Composites of Resorcinol Formaldehyde as Thermal Protection Systems for Re-Entry Vehicles. *RSC Adv.* **2014**, *4*, 28956–28963. [[CrossRef](#)]
24. Bauer, W.; Fox, C.; Gosse, R.; Perram, G. Visible Emission from C2 and CN During CW Laser-Irradiated Graphite. *Opt. Eng.* **2016**, *56*, 011017. [[CrossRef](#)]
25. Leone, C.; Mingione, E.; Genna, S. Laser cutting of CFRP by Quasi-Continuous Wave (QCW) fiber laser: Effect of process parameters and analysis of the HAZ index. *Compos. Part B-Eng.* **2021**, *224*, 109146. [[CrossRef](#)]
26. McWhorter, B.B.; Johnson, M.A.; Bryner, B.B.; Ewing, M.E. An instrument for real time measurement of solid rocket motor insulation erosion. In Proceedings of the 35th Joint Propulsion Conference and Exhibit, Los Angeles, CA, USA, 20–24 June 1999; p. 2136.
27. McWhorter, B.B.; Ewing, M.E.; Bolton, D.E.; Albrechtsen, K.U.; Earnest, T.E.; Noble, T.C.; Logaker, M. Real-Time Inhibitor Recession Measurements in Two Space Shuttle Reusable Solid Rocket Motors. In Proceedings of the 39th AIAA/ASME/SAE/ASEE Joint Propulsion Conference and Exhibit, Huntsville, AL, USA, 20–23 July 2003; p. 5107.
28. McWhorter, B.B.; Ewing, M.E.; Albrechtsen, K.U.; Noble, T.C.; Logaker, M. Real-Time Measurements of Aft Dome Insulation Erosion on Space Shuttle Reusable Solid Rocket Motor. In Proceedings of the 40th AIAA/ASME/SAE/ASEE Joint Propulsion Conference and Exhibit, Fort Lauderdale, FL, USA, 11–14 July 2004; p. 3896.
29. Cauty, F.; Demarais, J.C.; Erades, C.; Caugant, C. Internal insulation and solid propellant behavior measured by ultrasonic method on solid rocket motors. In Proceedings of the 33rd Joint Propulsion Conference and Exhibit, Seattle, WA, USA, 6–9 July 1997; p. 2994.
30. Sakai, T.; Nakazawa, H.; Dantsuka, Y.; Kitagawa, K.; Hirai, K. Dual-Component Sensor Design for In Situ Ablation Measurement. *J. Thermophys. Heat Transf.* **2017**, *31*, 307–317. [[CrossRef](#)]
31. Martin, H.T.; Cortopassi, A.C.; Kuo, K.K. Assessment of the Performance of Ablative Insulators Under Realistic Solid Rocket Motor Operating Conditions. *Int. J. Energ. Mater. Chem. Prop.* **2017**, *16*, 1–22. [[CrossRef](#)]
32. Zhe, Q.; Xian, W.; Yunlong, T.; Honghong, S.; Lianzhong, C.; He, G.; Xue, F. In Situ Visualization Measurement of Flat Plate Ablation in High-Temperature Gas Flow. *J. Appl. Mech.* **2018**, *85*, 061006.
33. Tang, Y.; Yue, M.; Zhang, J.; Li, Y.; Fang, X.; Feng, X. Revealing thermal ablation mechanisms of C/SiC with in situ optical observation and numerical simulation. *J. Eur. Ceram. Soc.* **2020**, *40*, 3897–3905. [[CrossRef](#)]
34. Zhu, S.; Zhang, J.; Yue, M.; Tang, Y.; Yue, W.; Qu, Z.; Wang, X.; Chen, L.; Gui, Y.; Feng, X. Ablation evolution of a new light weight silicon based thermal protection material in high-temperature gas flow. *Ceram. Int.* **2022**, *48*, 7136–7144. [[CrossRef](#)]
35. Meng, S.; Zhou, Y.; Xie, W.; Yi, F.; Du, S. Multiphysics coupled fluid/thermal/ablation simulation of carbon/carbon composites. *J. Spacecr. Rocket.* **2016**, *53*, 930–935. [[CrossRef](#)]
36. Schrooyen, P.; Turchi, A.; Hillewaert, K.; Chatelain, P.; Magin, T.E. Two-way coupled simulations of stagnation-point ablation with transient material response. *Int. J. Therm. Sci.* **2018**, *134*, 39–52. [[CrossRef](#)]
37. Ge, J.; Li, W.; Chao, X.; Wang, H.; Wang, Z.; Qi, L. Experiment-based numerical evaluation of the surface recession of C/C-SiC composites under the high-energy laser. *Ceram. Int.* **2022**, *48*, 34550–34563. [[CrossRef](#)]

38. Wang, Y.Q.; Shen, N.G.; Befekadu, G.K.; Pasiliao, C.L. Modeling pulsed laser ablation of aluminum with finite element analysis considering material moving front. *J. Heat Mass Transfer*. **2017**, *113*, 1246–1253. [[CrossRef](#)]
39. Wang, Y.Q.; Pasiliao, C.L. Modeling ablation of laminated composites: A novel manual mesh moving finite element analysis procedure with ABAQUS. *J. Heat Mass Transfer*. **2018**, *116*, 306–313. [[CrossRef](#)]
40. Wang, Z.; Wang, R.X.; Song, H.W.; Ma, T.; Wang, J.T.; Yuan, W.; Huang, C.G. Decoupling mechanisms of “avalanche” phenomenon for laser ablation of C/SiC composites in hypersonic airflow environment. *Int. J. Therm. Sci.* **2022**, *173*, 107414. [[CrossRef](#)]
41. Thielicke, W.; Stamhuis, E. PIVlab-towards user-friendly, affordable and accurate digital particle image velocimetry in MATLAB. *J. Open Res. Soft.* **2014**, *2*, e30. [[CrossRef](#)]
42. Zhao, W.N.; Song, H.W.; Huang, C.G.; Huang, Y.H. Modeling the Failure Behavior of CFRP Laminates Subjected to Combined Thermal and Mechanical Loadings. *Int. J. Appl. Mech.* **2017**, *9*, 1750033. [[CrossRef](#)]
43. Rose, N.; Le Bras, M.; Bourbigot, S.; Delobepb, R.; Castes, B. Comprehensive study of the oxidative degradation of an epoxy resin using the degradation front model. *Polym. Degrad. Stabil.* **1996**, *54*, 355–360. [[CrossRef](#)]
44. Rose, N.; Le Bras, M.; Bourbigot, S.; Delobel, R. Thermal oxidative degradation of epoxy resins: Evaluation of their heat resistance using invariant kinetic parameters. *Polym. Degrad. Stabil.* **1994**, *45*, 387–397. [[CrossRef](#)]
45. Kandare, E.; Kandola, B.K.; Staggs, J.E.J. Global kinetics of thermal degradation of flame-retarded epoxy resin formulations. *Polym. Degrad. Stabil.* **2007**, *92*, 1778–1787. [[CrossRef](#)]
46. Hu, J.; Xu, H.B.; Li, C. Laser absorption of carbon fiber reinforced polymer with randomly distributed carbon fibers. *Laser. Phys.* **2018**, *28*, 036002. [[CrossRef](#)]
47. Wang, J.T.; Ma, T.; Wang, Z.; Wang, R.X.; Song, H.W.; Yuan, W.; Zheng, H.W. Three-dimensional flow structures and heat transfer characteristics of compressible flow over a cylindrical cavity. *Aerosp. Sci. Technol.* **2022**, *122*, 107408. [[CrossRef](#)]

**Disclaimer/Publisher’s Note:** The statements, opinions and data contained in all publications are solely those of the individual author(s) and contributor(s) and not of MDPI and/or the editor(s). MDPI and/or the editor(s) disclaim responsibility for any injury to people or property resulting from any ideas, methods, instructions or products referred to in the content.